

A classical analogue for adiabatic Stark splitting in non-hydrogenic atoms

G W Gordon and F Robicheaux¹

Department of Physics, Auburn University, AL 36849, USA

E-mail: robichf@purdue.edu

Received 15 July 2013, in final form 10 October 2013

Published 11 November 2013

Online at stacks.iop.org/JPhysB/46/235003

Abstract

For highly excited low- ℓ states of atoms, a rising electric field causes a mixing between angular momenta that gives rise to Stark states. A relatively simple situation occurs if the electric field is not strong enough to mix states with adjacent principle quantum numbers. If the initial state has slightly lower (higher) energy than the degenerate manifold, then the state adiabatically connects to a Stark state with the electron on the low (high) potential energy side of the atom. We show that purely *classical* calculations for non-hydrogenic atoms have an adiabatic connection to extreme dipole moments similar to quantum systems. We use a simple map to show that the classical dynamics arises from the direction of the precession of the Runge–Lenz vector when the electric field is *off*. As a demonstration of the importance of this effect, we perform classical calculations of charge exchange and show that the total cross section for charge transfer and for ionization strongly depend on whether or not a pure Coulomb potential is used.

1. Introduction

The behaviour of a highly excited atom in an electric field has been studied since the dawn of quantum mechanics. Besides the experimental studies, there have been classical, semiclassical, and quantum treatments of this system. We give a brief survey of recent results. For example, [1, 2] describe fully classical treatments of H in weak electric fields. Reference [3] measured the Rb spectrum in a strong electric field and showed that there were resonance states above the classical threshold as well as above the zero-field threshold; a fully quantum treatment [4] gave quantitative agreement with this type of measurement. The non-hydrogenic part of the potential leads to strong changes from a purely hydrogenic case. A series of experiments and semiclassical and quantum calculations elucidated the importance of elastic scattering from the non-Coulombic part of the potential for the Stark spectra of atoms (some examples are [5–9]). In addition to time independent studies, there were several investigations based on time dependent motion of the electron probability (some examples are [10–14]). There are fewer purely classical studies of the non-hydrogenic Stark case; [15] investigated

how a small polarizability of the core affected the motion and [16] performed a classical calculation of how a non-hydrogenic atom is ionized in a low frequency microwave field. In many of the theoretical studies, a fully quantum treatment was compared to a semiclassical treatment; [17] investigated how the linear and the quadratic Stark shift in H compared between a quantum and a fully classical treatment.

In this study, we investigate how a classical non-hydrogenic atom responds to a slowly ramped electric field. An extreme example of this is state selective field ionization [18] in which the electron is eventually pulled from the atom; state selective field ionization is difficult to treat fully quantum mechanically [19] because of the long time scales involved. For electric fields that are not strong enough to mix states of different principle quantum number, an electric field gives eigenstates with an electric dipole moment that can have the electron on the high (low) potential energy side of the atom. These are states whose energy shifts up (down) with increasing electric field strength. If the electric field is in the $+z$ -direction, the high potential energy side of the atom for the electron has positive z .

The non-relativistic hydrogen atom is particularly simple in that the eigenstates only weakly depend on the electric field strength until the n -mixing regime. The situation is slightly more complicated for non-hydrogenic atoms [18].

¹ Present address: Department of Physics, Purdue University, West Lafayette, IA 47907, USA.

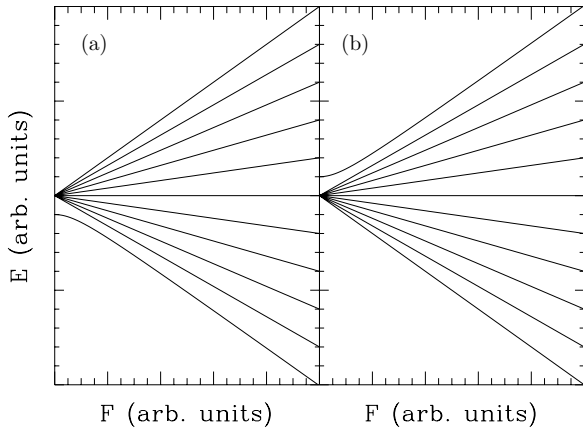


Figure 1. A schematic drawing for the electric field dependence of the energy levels of a non-hydrogenic atom with one state below (case (a)) or one state above (case (b)) a degenerate manifold.

Figure 1 shows two schematic cases for how energy levels vary as a function of electric field strength, F . The states with high angular momentum do not overlap with the non-Coulombic part of the potential and, thus, they behave similar to hydrogenic states: a small electric field induces a dipole moment which can have the electron either on the high or low potential energy side of the atom. This leads to a linear change of the energy with the electric field strength with the slope equal to minus the electric dipole moment. For the states that are not in the degenerate manifold, they connect to a Stark state that is on the low (high) potential energy side of the atom if the zero-field state is below (above) the degenerate manifold. When the electric field is large enough to mix the angular momenta, the variation of the energy with electric field strength is nearly linear indicating a nearly constant electric dipole moment. In most atoms, the low angular momentum states are below the degenerate manifold because atomic potentials are more attractive than pure Coulomb. However, there are cases where a state from a higher n falls just above the manifold for a lower n state (for example, the $\text{Ba}^+ nf$ -states) and these cases will behave as if the atomic potential is less attractive than pure Coulomb.

For this paper, we investigate how this system behaves when the calculation is performed classically. In particular, we are interested in how a classical low angular momentum state evolves in a slowly ramping electric field. There are many reasons why such a calculation could be interesting. One important reason is simply to see whether the classical calculation behaves similar to the quantum ([17] investigated the purely hydrogenic case for similar reasons). That is, do (almost) all classical trajectories with low angular momenta evolve to states with the electron having a time average on the correct side of the atom? For a test of this question, we solved the classical equations of motion for many low ℓ trajectories when the electron was subject to a spherical potential that was purely Coulombic, more attractive than Coulombic, or less attractive than Coulombic. We also wanted to understand the mechanism underlying the classical behaviour. Another reason to investigate this system is that there are situations where an atom, initially in low ℓ , is subject to a complicated interaction

where the quantum calculation is too difficult for current computational resources but the classical calculation can be performed. Thus, it is useful to know whether this property (how the low- ℓ states evolve with respect to a slowly increasing electric field) is present in a fully classical calculation.

We found that the classical motion mimicked the behaviour of the quantum system. If we used a purely Coulombic spherical potential, we found that the time average dipole moment along the electric field was approximately conserved as in the quantum case; this result has been known for a century. If we used a spherical potential that was more (less) attractive at short range than a pure Coulomb potential, we found that almost all of the trajectories evolved so that the average electron position was on the low (high) potential side of the atom *and* with nearly the maximum possible magnitude of dipole moment. Our results only apply to the classical analogue of the cases shown in figure 1 where the magnitude of the quantum defects is small; the classical analogue is that the precession of the Runge–Lenz vector from the non-Coulombic potential should give a small change in direction during one Rydberg period.

To understand this result, we surmised that the main features of the problem was the precession of the Runge–Lenz vector, \vec{A} , due to a non-Coulombic potential when the electric field is 0 *and* due to the rotation in the \vec{A}/\vec{L} space induced by the electric field. We were able to qualitatively reproduce the results of the full classical calculation using a simple map: rotation of \vec{A} in the plane perpendicular to the \vec{L} and a rotation between \vec{A} and \vec{L} perpendicular to the electric field. The direction of the precession of \vec{A} due to the non-Coulombic part of the potential depends on whether the potential is less or is more attractive than pure Coulomb; for \vec{L} in the z -direction, \vec{A} precesses clockwise (counter-clockwise) when the potential is less (more) attractive than pure Coulomb. *The direction of precession of \vec{A} from the non-Coulombic potential determines whether it evolves to be parallel or anti-parallel to the electric field.*

There have been many theoretical studies of the effect of a non-Coulombic potential on the spectra of atoms in external fields (e.g. see [5, 7, 20, 21]). These studies have found that the ‘scattering’ from the non-Coulombic core in alkali atoms could lead to quite complex behaviour. In these treatments, either one finds that the electron emerges in random directions from a quantum scattering event with the core or one finds that the scattering angle depends sensitively on the impact parameter (i.e. angular momentum) of the electron. This means the direction of the major axis of the ellipse for the electron goes to a random or nearly random direction. This sensitivity arises because they are treating the case where the change in the angular momentum during one Rydberg period is large or the quantum defects are large. In contrast, we are treating the situation where the change in angular momentum due to the external field is small during a Rydberg period and the electron trajectory is such that the states mixed by the electric field would all have small quantum defects (see figure 1). Because of these restrictions, the electron acquires only a small scattering angle each time the electron returns to small r and the value of the scattering angle smoothly changes. The main findings in

this paper would need to be revisited if the electron starts with small angular momentum so that the scattering angle is large and sensitively dependent on the precise value of the impact parameter *or* the field is so large that the change in angular momentum during one Rydberg period is sufficient to take the electron from large angular momentum (where the scattering angle is small and not sensitive) to small angular momentum (where the scattering angle is large and sensitive).

To show that this result can be important in practice, we performed classical calculations of ion–atom scattering. As with studies of the simple Stark effect, ion–atom scattering for highly excited states has a long history. For example, [22–24] experimentally studied *ℓ*-changing and *n*-changing collisions as well as charge transfer. Several theoretical studies [25–29] have investigated most aspects of this system. In the last section, we investigate charge transfer and ionization in ion–atom scattering where the target atom is initially in a low angular momentum state. The early stages of the scattering involve weak and slowly varying electric fields which can induce the electron to adiabatically connect to either red or blue Stark states depending on the initial quantum defect. We found that even the total cross sections depended on whether the target atom had a pure Coulomb potential or whether the potential was more or was less attractive than pure Coulomb. This effect does not appear to have been noticed previously.

2. Classical model

The classical equations of motion can be solved with a variety of techniques. We used an adaptive step-size Runge–Kutta method based on the one described in [30]. With this method, we solve the six coupled, first-order differential equations. As a consistency check in the calculations, we make sure that any conserved quantity changes by less than a part in 10^5 . As an additional check and for the cases where there were no conserved quantities, we compared distributions of physical parameters at the end of runs using different levels of convergence.

We chose a simple form for the non-Coulombic potential which allowed us to smoothly vary from more attractive, to pure Coulomb, to less attractive. The form we chose for the potential energy was

$$V(r) = -\frac{e^2}{4\pi\epsilon_0} \frac{1 + C \exp(-r/a_0)}{r} \quad (1)$$

where a_0 is the Bohr radius and C is an adjustable constant. When $C > 0$ ($C < 0$), the potential is more (less) attractive than pure Coulomb. Of course, the case of $C = 0$ is hydrogen. We only show results below for the cases $C = 1, 0$, and -1 although we did check that other values gave similar results.

The motion of an electron in a non-Coulombic potential and an electric field is complicated, but we found the Runge–Lenz vector facilitated an understanding of the motion. In our discussions below, we use the *scaled* Runge–Lenz vector

$$\vec{A} = \left(\vec{p} \times \vec{L} - m \frac{e^2}{4\pi\epsilon_0} \hat{r} \right) / \sqrt{-2mE} \quad (2)$$

where \vec{p} is the electron’s momentum, m is the electron mass and E is the energy of the electron. With this definition, the

\vec{A} points in the direction of the perihelion and has units of angular momentum. For a pure Coulomb potential, the Runge–Lenz vector is a constant of the motion. Two non-Coulombic interactions are important for understanding our results.

For a weak electric field in the z -direction, the angular momentum and the Runge–Lenz vectors rotate into each other:

$$\begin{aligned} \frac{d\vec{L}}{dt} &= -\omega \hat{z} \times \vec{A} \\ \frac{d\vec{A}}{dt} &= -\omega \hat{z} \times \vec{L} \end{aligned} \quad (3)$$

where $\omega = 3ea_0nF/(2\hbar)$ with n the principle quantum number and F the electric field strength. From these equations, one can show that L_z and A_z are constants in a weak electric field. The electric field gives a rotation in A_x and L_y :

$$\begin{aligned} L_y(t) &= L_y(0) \cos(\omega t) - A_x(0) \sin(\omega t) \\ A_x(t) &= L_y(0) \sin(\omega t) + A_x(0) \cos(\omega t) \end{aligned} \quad (4)$$

with similar rotation for A_y and L_x .

The other non-Coulombic interaction is from the spherical potential for the electron for non-hydrogenic atoms. The spherical potential does not change the angular momentum with time. However, it does give a rotation of the Runge–Lenz vector in a plane perpendicular to the angular momentum during each radial period. If the angular momentum is in the y -direction, the equation of motion $d\beta/dt = L_y/(mr^2)$ can be used to show that over a radial period the change in angle of the Runge–Lenz vector is

$$\Delta\beta = 2 \int_{r_{\min}}^{r_{\max}} \frac{L_y}{r^2 p(r)} dr - 2\pi \quad (5)$$

where we used $dt = dr/[p(r)/m]$, r_{\min} is the inner turning point, r_{\max} is the outer turning point, and $p(r) = \sqrt{2m[E - V_{\text{eff}}(r)]}$ is the radial momentum with $V_{\text{eff}} = V_{\text{atom}}(r) + L_y^2/(2mr^2)$. Using this notation, after each radial period the Runge–Lenz vector rotates as

$$\begin{aligned} A_z(T_{\text{Ryd}}) &= A_z(0) \cos(\Delta\beta) - A_x(0) \sin(\Delta\beta) \\ A_x(T_{\text{Ryd}}) &= A_z(0) \sin(\Delta\beta) + A_x(0) \cos(\Delta\beta) \end{aligned} \quad (6)$$

where T_{Ryd} is the Rydberg period. For the general case, $|\vec{L}|$ replaces the L_y in equation (5) and the sense of rotation follows the right hand rule in the plane perpendicular to \vec{L} .

Figure 2 shows how $\Delta\beta$ depends on angular momentum for the potentials with $C = 1$ (solid line) and $C = -1$ (dotted line). For the potential more attractive than pure Coulomb ($C = 1$), there is a maximum in the precession angle at $\ell_y = L_y/\hbar \sim 1.5$. The case $C = -1$ is special in that it does not have a singularity at $r = 0$ (although there is a discontinuity in the derivative); this allows the electron to go straight through the origin for $L_y = 0$ which is why $\Delta\beta \rightarrow -\pi$ as $L_y \rightarrow 0$.

A last important feature is that the classical solution gives the same answer for the same starting condition. Therefore, we needed to make sure our results did not depend on the specific choice of our initial condition. For a given starting position and velocity, we averaged over the phase of the electron orbit by

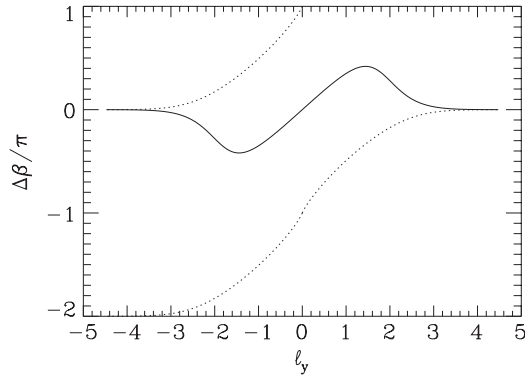


Figure 2. The change in angle per Rydberg period as a function of $\ell_y \equiv L_y/\hbar$ for the case $C = 1$ (solid line) and the case $C = -1$ (dotted line). Note there are three ways to connect the region of negative angular momentum to positive angular momentum: (a) $\Delta\beta(-\ell_y) = -\Delta\beta(\ell_y)$, (b) $\Delta\beta(-\ell_y) = 2\pi - \Delta\beta(\ell_y)$, or (c) $\Delta\beta(-\ell_y) = -2\pi - \Delta\beta(\ell_y)$. Only one case gives continuity through the point $\ell = 0$. For the $C = 1$ potential, method (a) gives continuity. For the $C = -1$ potential, method (c) gives continuity (also shown is method (a)).

running the field free case for a random fraction of a Rydberg period. We also made sure that the initial orientation of the orbit was not important. For a specified angular momentum ℓ , we started the position at a random spot on the sphere defined by the aphelion with a flat distribution in $\cos(\theta)$ and in ϕ . To ensure a random orientation of the plane of motion with the electric field set to 0, the velocity vector is chosen from a random distribution $\vec{v} = (\hat{\theta} \cos \alpha + \hat{\phi} \sin \alpha)v$ where α is chosen from a random distribution.

3. Ramped electric field results: full classical

In this section, we present the results of our calculations where we slowly ramped on an electric field to a constant value. A worry is that the electric field should smoothly turn on to avoid artefacts from discontinuities in the time derivative of the Hamiltonian. To avoid this we chose the time dependent electric field to have a similar form from [31]:

$$F(t) = \frac{t_{\text{wid}}}{t_{\text{flat}}} F_{\text{max}} \ln \left(\frac{1 + e^{t/t_{\text{wid}}}}{1 + e^{(t-t_{\text{flat}})/t_{\text{wid}}}} \right) \quad (7)$$

where t_{wid} gives the effective time width over which the field ramps on, t_{flat} is approximately the time where the field becomes constant and where F_{max} is the maximum electric field. This functional form has the property that it smoothly increases from 0 as t approaches 0 from below and then smoothly becomes a linear function of time when t is larger than t_{wid} . It then smoothly changes to a constant near the time $t \sim t_{\text{flat}}$.

In the calculations of this section, we chose $t_{\text{wid}} = 500T_{\text{Rydberg}}$ (i.e. 500 Rydberg periods) and $t_{\text{flat}} = t_{\text{wid}}$. Our results were not sensitive to these values as long as the Runge–Lenz vector can precess many times during the ramp. This condition is the same as in the quantum atom. If the electric field is turned on too rapidly, the states do not evolve adiabatically. In all of the cases, the maximum electric field strength was 250 V m^{-1} (i.e. 2.5 V cm^{-1}).

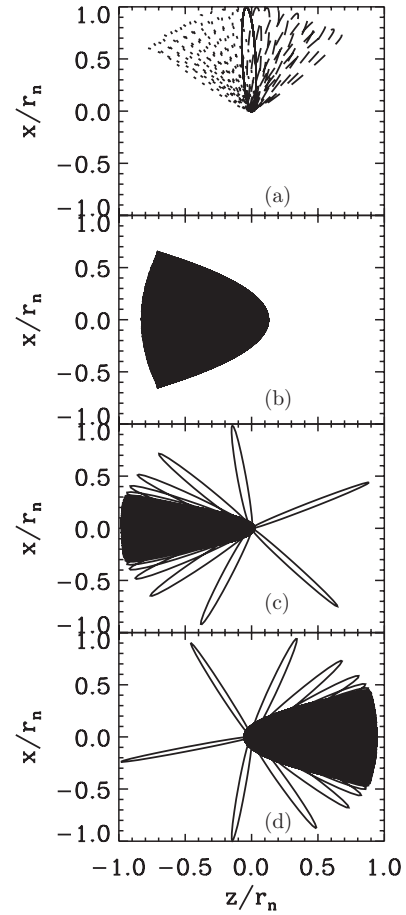


Figure 3. Trajectories in the zx -plane scaled by the atom size $r_n = 2n^2 a_0$. For all cases, $L_y > 0$ which means the angular momentum is out of the page. (a) Trajectories for ~ 10 Rydberg periods when the electric field is 0: the case $C = 0$ (solid line) is a single ellipse nearly vertical, the case $C = 1$ (dotted line) gives an ellipse precessing counter-clockwise, and the case $C = -1$ (dashed line) gives an ellipse precessing clockwise. (b) Trajectories for ~ 200 Rydberg periods showing the precession due to an electric field in the z -direction for $C = 0$. The z -component of the Runge–Lenz vector is conserved. The points of the trajectory are so dense it shows up as a black wedge instead of separate lines. (c) Same as (b) but for $C = 1$. The Runge–Lenz vector is no longer constant. There are ~ 8 Rydberg periods over which the direction of the major axis rotates counter-clockwise from $\sim -25^\circ$ to $\sim 25^\circ$ relative to the $-z$ -axis. (d) Same as (c) but for $C = 1$. Now the direction of the major axis rotates clockwise from $\sim -30^\circ$ to $\sim 30^\circ$ relative to the z -axis during ~ 7 Rydberg periods.

To become oriented with how the classical electron behaves, figure 3 shows six example trajectories: figure 3(a) shows trajectories with the electric field off for $C = 0, -1$, and 1 while 3(b)–(d) show trajectories with an electric field in the z -direction. For all plots, the angular momentum is initially out of the page; only for figure 3(b) is the angular momentum into the page for part of the trajectory. The case with no electric field, figure 3(a), shows the precession due to a non-Coulombic force compared to the trajectory for pure Coulomb which is an ellipse slightly left of vertical; the $C = 1$ case gives counter-clockwise precession because the potential is deeper than pure Coulomb while the $C = -1$ case gives clockwise precession. Figure 3(b) shows the trajectory for pure Coulomb plus electric

field in the z -direction. The trajectory has too many lines to see the individual ellipses; qualitatively the major axis of the ellipse oscillates within the black wedge with the minimum angular momentum at the edge of the wedge. Figure 3(c) shows the $C = 1$ case with an electric field in the z -direction; this is a late time part of the trajectory that arose from slowly ramping on the electric field. Note that the electron is on the low potential energy side of the atom for most of the trajectory. There is a very rapid swing of the major axis around the atom in the counter-clockwise direction over a short period of time, ~ 8 Rydberg periods. Figure 3(d) shows the $C = -1$ case that arose from slowly ramping on the electric field. Now the electron is on the high potential energy side of the atom for most of the trajectory. Again, there is a rapid swing of the major axis around the atom, but now in the clockwise direction.

Figure 4 shows the results from three typical trajectories for $n = 30$ using the parameters L_y , A_x and A_z to help visualize the dynamics. It is important to remember that the angular momentum and Runge–Lenz vector satisfy the relation $|\vec{L}|^2 + |\vec{A}|^2 = n^2\hbar^2$. For all of the trajectories in figure 4, we chose the initial conditions so that the orbit was in the xz -plane which means only L_y , A_x and A_z are non-zero; because the electric field is in the z -direction, the quantities L_x , L_z , and A_y remain zero for this calculation. This figure shows the cycle average of these quantities (that is, we averaged over one Rydberg period) scaled by \hbar . The different figures all show the case where the initial $\ell_y = 3$, $A_z \simeq 1.2\hbar$ and $A_x \simeq -30\hbar$ but with $C = 0$ (figure 4(a)), $C = 1$ (figure 4(b)), and $C = -1$ (figure 4(c)). From equation (1), figure 4(a) corresponds to pure Coulomb, figure 4(b) corresponds to more attractive than pure Coulomb, and figure 4(c) corresponds to less attractive than pure Coulomb.

Figure 4(a) is the pure Coulomb case which shows that $a_z = \langle A_z \rangle / \hbar$ is nearly constant even when the electric field ramps on. The $a_x = \langle A_x \rangle / \hbar$ and $\ell_y = \langle L_y \rangle / \hbar$ show a more complicated behaviour. As the electric field ramps on, these two parameters oscillate with a frequency that increases as the electric field increases. As seen from equation (4), the ℓ_y reaches the maximum value ahead of the a_x ; the oscillations of these parameters are 90° out of phase to satisfy the condition $|\vec{\ell}|^2 + |\vec{a}|^2 = n^2$.

The $C = 1$ case (deeper than Coulomb potential), figure 4(b), demonstrates a richer behaviour. When the electric field is approximately 0 (for $t/T_{\text{Ryd}} < -500$), the ℓ_y is a constant and the two components of the Runge–Lenz vector oscillate due to the precession of the orbit in the xz -plane. As the electric field increases, a more complicated motion ensues; see figure 3(c) for part of the trajectory in $z-x$. The a_z goes to a large, positive value which is nearly constant except for some sharp dips; the frequency of these dips increase with increasing electric field, but they also become sharper with increasing electric field. The dips correspond to the part of figure 3(c) where the major axis swings around the atom and the nearly constant a_z corresponds to the dark wedge. Note that a positive a_z means the electron is on the negative z side of the atom which is the *low* potential side; also, the fact that $a_z \sim 30$ means that the electron has nearly the maximum allowed dipole moment for this energy. This is analogous to what happens in the fully

quantized atom (figure 1(a)). The a_x and ℓ_y have a different kind of behaviour. The ℓ_y has a half oscillation; it increases from a small value, but, when it returns to the small value, the ℓ_y ‘reflects’ and begins another oscillation; unlike the pure Coulomb case, the ℓ_y stays positive. The a_x approximately linearly increases until it suddenly spikes to large positive value, quickly followed by a flip in sign, with a jump back to a medium negative value, after which it approximately linearly increases again.

This behaviour can be understood by the motion encapsulated in figure 4(a) modified by the non-Coulombic spherical potential. When ℓ_y is larger than ~ 2 , the electron behaves like it is in a pure Coulomb potential plus uniform electric field: a_z is nearly constant while there is uniform rotation in the a_x and ℓ_y space. For example, when ℓ_y is near its maximum, the a_x should be linearly increasing (see the time $t \sim 2200T_{\text{Ryd}}$ in figure 4(a)). As ℓ_y decreases toward 0, the precession from the non-Coulombic spherical potential dominates. This causes a rapid precession between a_z and a_x . As the a_z approaches its maximum value from below, the a_x is increasing from the most negative value, -30 . When $a_x \sim -10$, then the ℓ_y and a_x can again form a freely rotating pair in the electric field.

The $C = -1$ case (shallower than Coulomb potential), figure 4(c), illustrates similarly rich behaviour. Again, when the electric field is approximately 0 (for $t/T_{\text{Ryd}} < -500$), the ℓ_y is a constant and the two components of the Runge–Lenz vector oscillate due to the precession of the orbit in the xz -plane. However, the rotation direction is reversed compared to the $C = 1$ case. When the electric field has sufficiently increased, a situation similar to that in figure 4(b) results *except that the a_z goes to a large negative value*; see figure 3(d) for part of the trajectory in $z-x$. A negative a_z means the electron is on the positive z side of the atom which is the *high* potential side; also, the fact that $a_z \sim -30$, means that the electron has nearly the maximum allowed dipole moment for this energy. This is analogous to what happens in the fully quantized atom (figure 1(b)). The complicated motion for $t > 0$ can be explained in a similar manner to figure 4(b).

Figure 4 is one of the main results of this paper. It shows that the adiabatic connection between the low field states and high field states is also present in a fully classical calculation: deeper (shallower) than Coulomb potentials lead to adiabatic connection to a dipole on the low (high) potential side of the atom. We found this behaviour in a wide range of calculations. There were systematics that are worth noting. For a given potential, larger ℓ_y typically required smaller electric fields to go to these classical ‘Stark’ states and required longer ramp times; this is similar to quantum calculations since the higher ℓ are more easily mixed with the degenerate manifold but the adiabaticity condition is more easily violated.

There is a situation where the classical-quantum correspondence becomes problematic. When the potential becomes substantially different than Coulomb, the magnitude of the quantum defect can become larger than $1/2$ and/or the change in the angle β can have a magnitude larger than π . For this case, the low- ℓ state is shifted so far from the degenerate n -manifold that it might not mix with those states in a simple way.

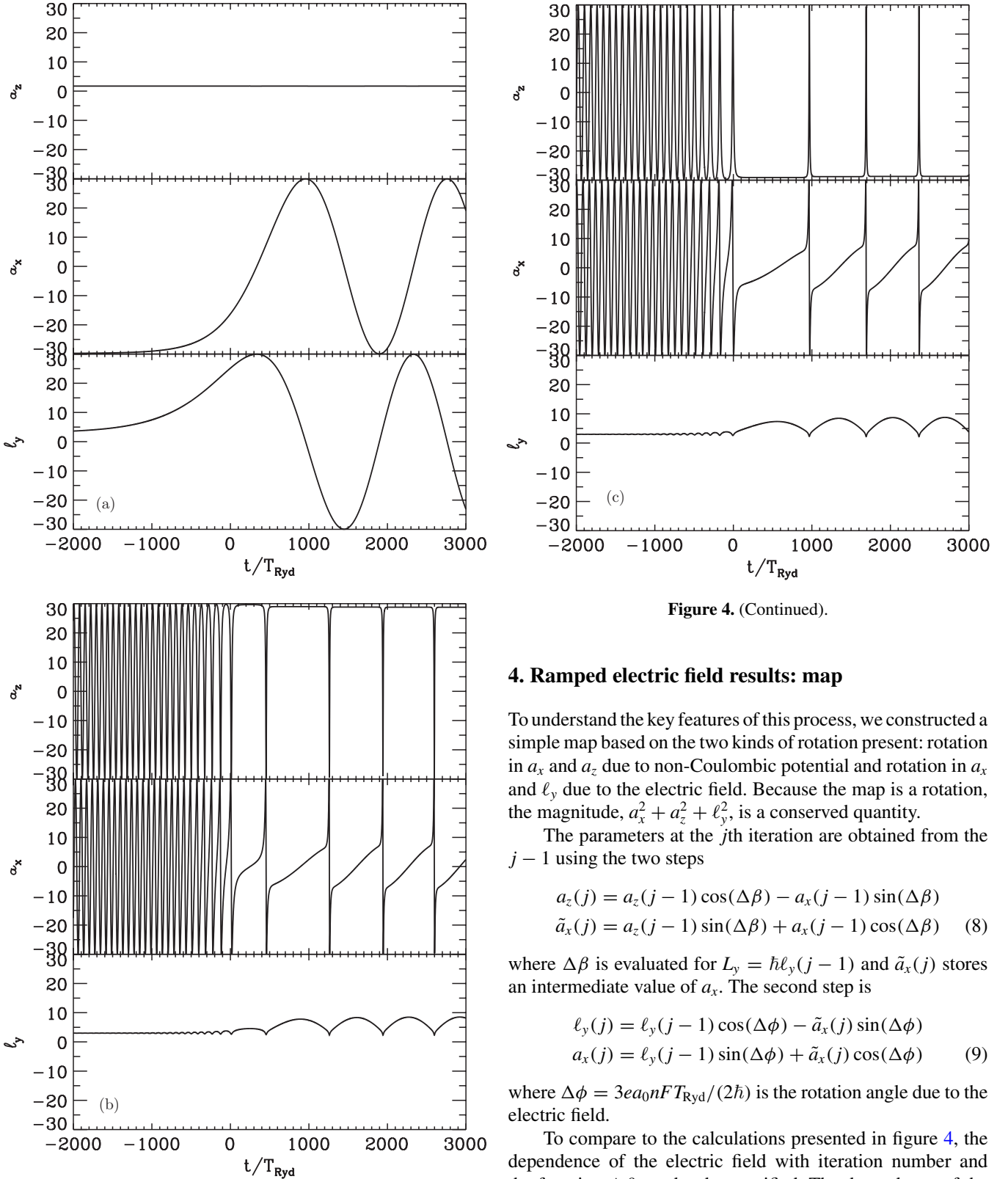


Figure 4. (Continued).

4. Ramped electric field results: map

To understand the key features of this process, we constructed a simple map based on the two kinds of rotation present: rotation in a_x and a_z due to non-Coulombic potential and rotation in a_x and l_y due to the electric field. Because the map is a rotation, the magnitude, $a_x^2 + a_z^2 + l_y^2$, is a conserved quantity.

The parameters at the j th iteration are obtained from the $j - 1$ using the two steps

$$\begin{aligned} a_z(j) &= a_z(j-1) \cos(\Delta\beta) - a_x(j-1) \sin(\Delta\beta) \\ \tilde{a}_x(j) &= a_z(j-1) \sin(\Delta\beta) + a_x(j-1) \cos(\Delta\beta) \end{aligned} \quad (8)$$

where $\Delta\beta$ is evaluated for $L_y = \hbar l_y(j-1)$ and $\tilde{a}_x(j)$ stores an intermediate value of a_x . The second step is

$$\begin{aligned} l_y(j) &= l_y(j-1) \cos(\Delta\phi) - \tilde{a}_x(j) \sin(\Delta\phi) \\ a_x(j) &= l_y(j-1) \sin(\Delta\phi) + \tilde{a}_x(j) \cos(\Delta\phi) \end{aligned} \quad (9)$$

where $\Delta\phi = 3ea_0nFT_{\text{Ryd}}/(2\hbar)$ is the rotation angle due to the electric field.

To compare to the calculations presented in figure 4, the dependence of the electric field with iteration number and the function $\Delta\beta$ need to be specified. The dependence of the electric field is simply as in equation (7) but with the time defined to be $t = jT_{\text{Ryd}}$. For the $\Delta\beta$, we fit the numerical calculation in figure 2 to simple functions. The simplest is $\Delta\beta = 0$ for $C = 0$. The $C = 1$ function was taken to be $\Delta\beta = 1.2l_y \exp(-|l_y^3|/16)/(1 + l_y^6/100)$. The $C = -1$ function was taken to be $\Delta\beta = -\pi \exp(-0.7l_y - l_y^3/20)$ for $l_y > 0$ and $\Delta\beta(l_y) = -\Delta\beta(-l_y)$ for $l_y < 0$.

Figure 4. The evolution of the cycle average parameters divided by \hbar : $l_y = \langle L_y \rangle / \hbar$, $a_x = \langle A_x \rangle / \hbar$, and $a_z = \langle A_z \rangle / \hbar$.

In this case, how the state evolves depends on the relative position of more than one low- l state. We do not expect the straightforward treatment of this paper will hold in that case.

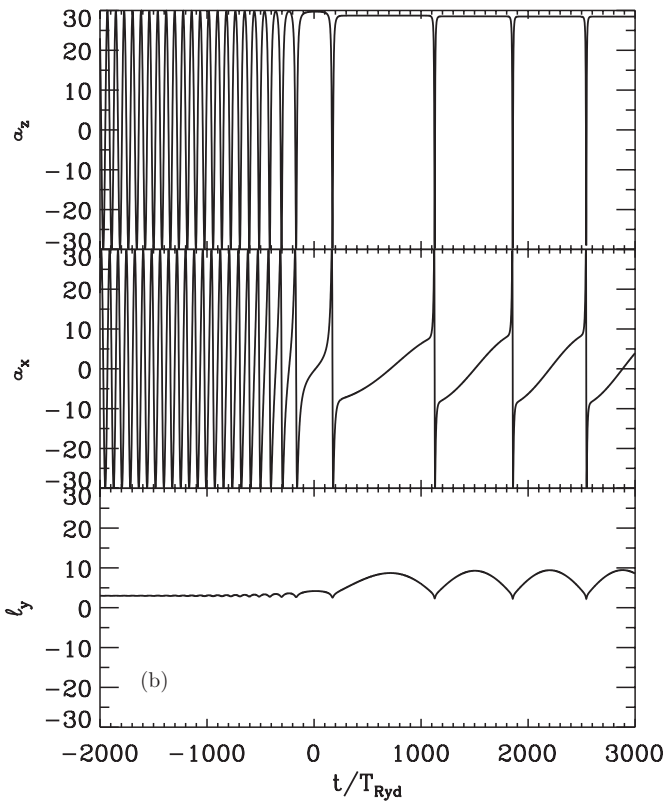
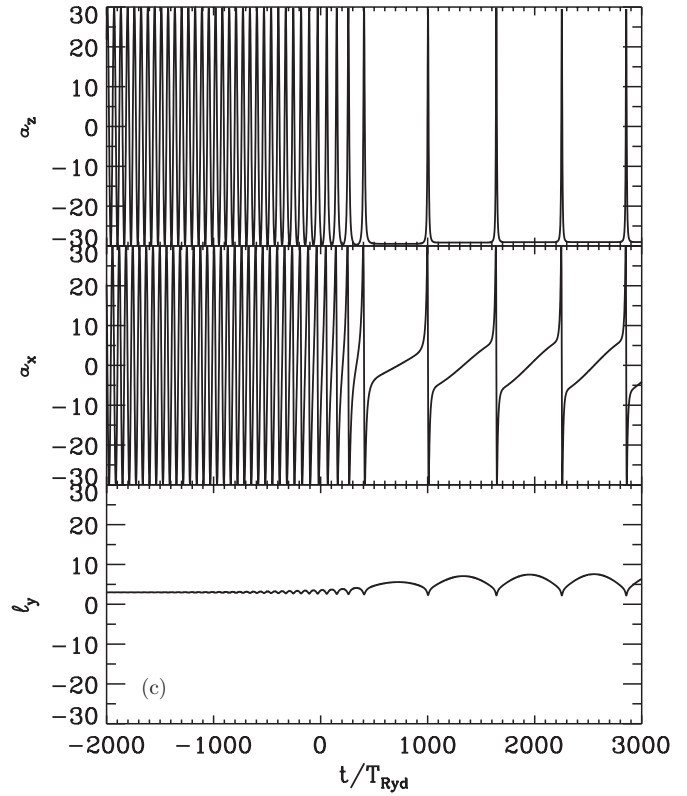
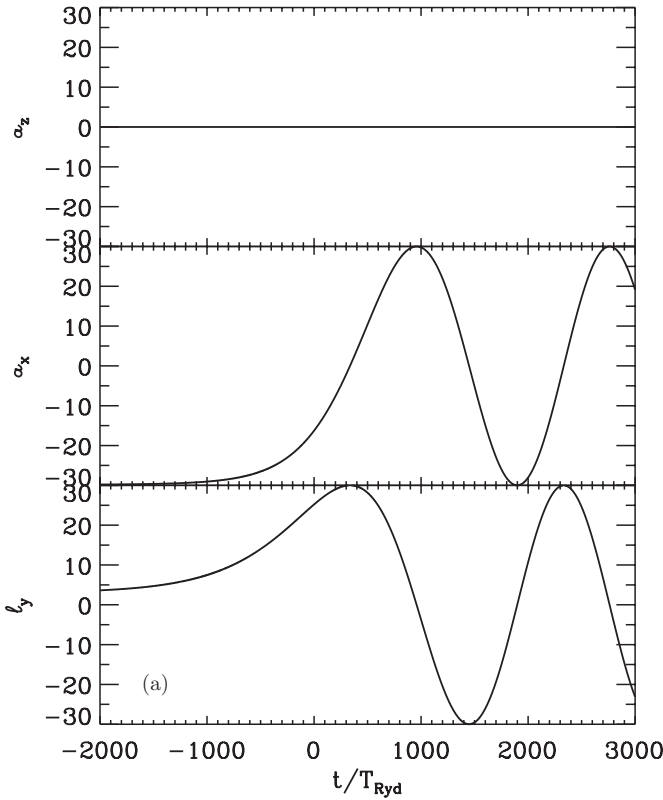


Figure 5. (Continued.)

Figure 5. Same as figure 3 but calculated using the map.

Results are shown in figure 5 for calculations done with similar initial conditions to those in figure 4. It is clear that the map gives similar results to the full calculation. The $C = 0$ case is most similar because there is hardly any approximation

for a pure Coulomb potential. The $C = 1$ and $C = -1$ do not give results identical to that for the full calculation but this should not be expected considering the simplicity of the map and our approximations for $\Delta\beta(L_y)$. However, there is the same qualitative behaviour in *all* of the parameters. For $C = 1$ (figures 4(b) and 5(b)), the a_z adiabatically evolves to nearly the maximum value of 30 except for regions where it sharply dips down to ~ -30 . The $C = -1$ case (figures 4(c) and 5(c)) has the a_z near -30 except for the sharp spikes up to ~ 30 . Thus, it appears that this simple map captures the essential features of the full calculation. The a_x and l_y also have similar behaviour in figures 4 and 5 demonstrating that the map encompasses the main features of this system.

We can use the map to help visualize how the system evolves. Because the three variables (a_x, l_y, a_z) have an invariant norm ($\sqrt{a_x^2 + l_y^2 + a_z^2} = n$) in the map, we can plot how an initial condition evolves on a sphere. Figure 6 shows how the angle on the sphere evolves for different initial conditions when the electric field is held fixed at 250 V m^{-1} ; the angles are defined as $\cos(\eta) = a_z/n$ and $\tan(\xi) = l_y/a_x$. The starting condition is chosen to have either $\xi = \pi/2$ or $\xi = -\pi/2$ and our set of initial $\cos(\eta)$ was chosen to be $-0.95, -0.9, -0.8, -0.6, \dots, 0.6, 0.8, 0.9, \text{ and } 0.95$. Figure 6(a) shows the case where $C = 0$. For this situation, the electric field causes a rotation between a_x and l_y keeping a_z fixed. This leads to vertical lines. For our definitions, ξ decreases until it reaches $-\pi$ at which point it is reset to π . Figure 6(b) shows the case where $C = 1$. The trajectory evolves by ξ decreasing until it is near either 0 or -1 . When ξ is near an integer multiple of π , the l_y is small. This triggers a precession in a_x and a_z so

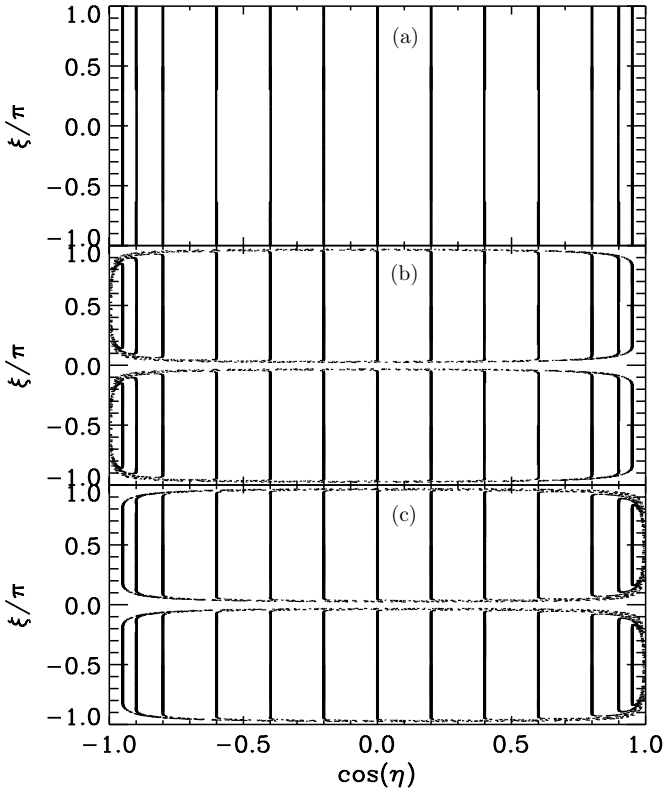


Figure 6. Evolution of the parameters (a_x, l_y, a_z) for different initial conditions when $F = 250 \text{ V m}^{-1}$. The parameters in the plot are defined as $\cos(\eta) = a_z / \sqrt{a_x^2 + l_y^2 + a_z^2}$ and $\tan(\xi) = l_y / a_x$. Case (a) is for $C = 0$, (b) is for $C = 1$, and (c) is for $C = -1$. For all cases, the initial condition was for $\cos(\eta)$, ξ/π equal to $(-0.95, 0.5)$, $(-0.9, 0.5)$, $(-0.8, 0.5)$, $(-0.6, 0.5)$, \dots , $(0.6, 0.5)$, $(0.8, 0.5)$, $(0.9, 0.5)$, $(0.95, 0.5)$ and for the same points but with ξ/π changed from 0.5 to -0.5 .

that $\cos(\eta)$ decreases to ~ -1 . At this point, the ξ increases by a little less than π at which point the $\cos(\eta)$ increases to its original value. After which, ξ decreases again keeping $\cos(\eta)$ approximately fixed. Taking the earth as a model, the trajectory follows constant latitude until it nears the great circle defined by $\xi = 0$ or $\xi = \pi$, it then moves around the earth keeping approximately the same distance from this great circle until it reaches its original latitude, after which the motion repeats. Figure 6(c) shows the case where $C = -1$. The motion is similar with the only difference being that the $\cos(\eta)$ increases when ξ nears 0 or -1 from above followed by ξ increasing by $\sim \pi$, after which $\cos(\eta)$ decreases until it reaches its original value.

5. Charge transfer results

To show that the non-Coulombic atomic potential could affect an important physical process, we computed the charge transfer and ionization cross sections for ions hitting an atom in a Rydberg state. We performed the calculations for the $C = 1$, $C = 0$ and $C = -1$ potentials.

In these calculations, we start the ion at an initial position $(b_x, b_y, z_{\text{init}})$ where the b_x, b_y are from a flat distribution within the circle defined by b_{max} . The b_{max} is chosen so that all of the trajectories that end with ionization or charge transfer

are within a smaller circle defined by $0.95b_{\text{max}}$ (for most calculations all ionization or charge transfers were within a circle defined by $0.85b_{\text{max}}$). The total cross section for a process is the fraction of runs that end in that process times the area πb_{max}^2 . The cross section calculation was performed for a specified starting angular momentum L and binding energy but with all other orbital parameters being random.

A difficulty with this kind of calculation is that the ion should start far from the atom and continue far past the atom. In order to speed up the convergence with respect to the distance that we started the ion, we used the time dependent factor in equation (7) to smoothly turn on the charge of the ion:

$$Z(t) = Z \ln \left(\frac{1 + e^{(t-t_0)/t_{\text{wid}}}}{1 + e^{(t-t_0-t_{\text{wid}})/t_{\text{wid}}}} \right) \quad (10)$$

where Z is the charge of the ion, $t_0 = z_0/v_{\text{ion}} - 7t_{\text{wid}}$ is roughly the time at which the ion charge turns on, and we used $t_{\text{wid}} = 10T_{\text{Ryd}}$. The position of the ion in time was given by the vector $(b_x, b_y, v_{\text{ion}}t)$ so that $t = 0$ is the time of closest approach. We started the simulation at random times so the electron would be at random phases of its orbit. The initial time was chosen to be $t_{\text{init}} = z_0/v_{\text{ion}} - 14t_{\text{wid}} - t_{\text{wid}} \times \text{ran}$ where ran was a random number from a flat distribution between 0 and 1 . This time is chosen so that the ion charge is initially less than 0.0006 of its full value and is at $\simeq 0.9984$ of its full value when the ion is at the position z_0 . Finally, calculations were done for three different z_0 to test for convergence: $z_0 = 400n^2a_0$, $800n^2a_0$, and $1600n^2a_0$ where n is the principle quantum number for the atom. We found that our results were similar for all three z_0 which indicates convergence with respect to initial distance. For the total cross sections, the number of charge transfer plus the number of ionization trajectories was 8000 for each ion speed. For the differential cross sections, the number of charge transfer trajectories was $24\,000$.

Figure 7 shows the total charge transfer and the total ionization cross section for the different atomic potentials as a function of ion speed for an initial $L = 1.5\hbar$. For this figure, the ion charge is 3 and the atom starts with an energy corresponding to that for $n = 12$. At lower ion speeds, the $C = 1$ charge transfer cross section is larger than that for $C = 0$ which is larger than that for $C = -1$. This difference arises because, while it is on the atom, the electron adiabatically connects to the low (high) potential side of the atom for $C = 1$ ($C = -1$). For ion scattering, the low potential side of the atom is the same side as the ion. Thus, for $C = 1$ ($C = -1$), the electron is close to (far from) the ion as it passes. This facilitates the charge transfer for $C = 1$ and suppresses it for $C = -1$. At high ion velocities, there is not a large difference between the potentials because the Runge–Lenz vector cannot precess fast enough to track the ion. There is a similar difference in the ionization cross section but it is not quite as pronounced because the ionization is largest for the highest ion speed in our plot.

Figure 8 shows the energy distribution of the captured electron for the ion speed of $1.5 \times 10^5 \text{ m s}^{-1}$ in figure 7(a) and $2.5 \times 10^5 \text{ m s}^{-1}$ in figure 7(b); these speeds correspond to scaled speeds of 0.82 and 1.37 of figure 7. The initial binding energy of the atom is $E = -0.5/12^2 \simeq -0.094 \text{ eV}$ and the initial angular momentum was taken to be $1.5\hbar$ as in figure 7. In

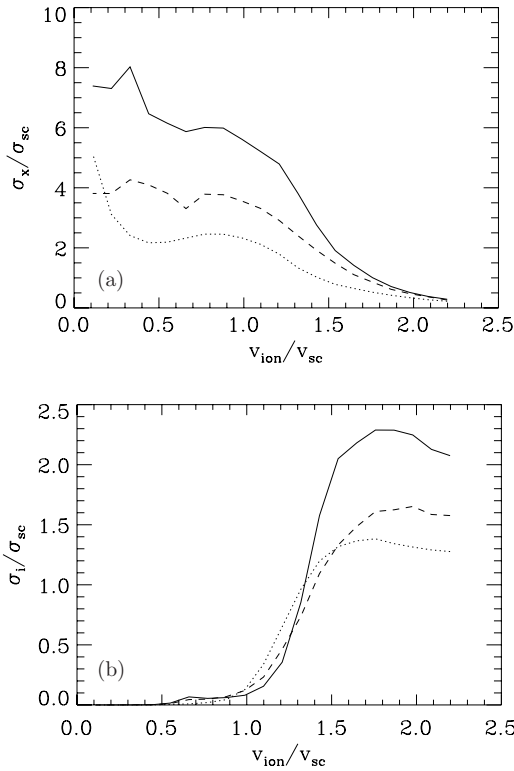


Figure 7. The charge transfer cross section (σ_x in (a)) and the ionization cross section (σ_i in (b)) versus the ion speed. The cross sections have been scaled by the geometric cross section, $\pi(2n^2a_0)^2 \simeq 7.30 \times 10^{-12} \text{ cm}^2$, and the ion speed has been scaled by the average electron speed, $\alpha c/n \simeq 1.82 \times 10^5 \text{ m s}^{-1}$. In both plots, the cross section when the potential is more attractive than Coulombic ($C = 1$) is the solid line, when the potential is Coulombic ($C = 0$) is the dashed line, and when the potential is less attractive than Coulombic ($C = -1$) is the dotted line.

figure 7, the charge transfer cross section at these two energies was largest for $C = 1$ and smallest for $C = -1$ which is reflected in the energy distributions of figure 8. At the lower speed, the charge transfer energy distribution is peaked near the initial binding energy of the atom, but, at the higher speed, the energy distribution rises until the threshold is reached. This has been seen in previous calculations and experiments. It is interesting that the energy distributions have quite different shapes at the lower speed. Also, most of the difference between the different curves occurs between -0.2 and -0.08 eV . It appears that the mechanism that gives charge transfer with *large* energy change behaves similarly for all calculations at the lower speed. At the higher speed, the shapes are more similar but the size is different.

We also computed the angular momentum distribution of the transferred electron. There were some differences resulting from the different potentials. The $C = 1$ case had a distribution that (roughly) linearly increased until $\sim 30\hbar$ after which it rapidly decreased whereas the $C = -1$ case (roughly) linearly increased with a smaller slope until $\sim 20\hbar$ after which it slowly decreased to 0 at $\sim 40\hbar$.

We performed charge transfer and ionization calculations for larger initial L ($2.5\hbar$ and $3.5\hbar$). We found that when L increased the results for the different potentials become similar to each other. This is not surprising because the differences

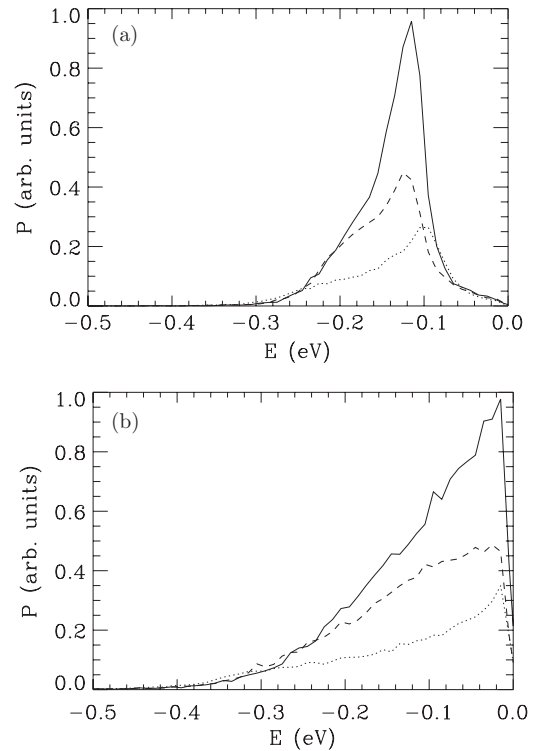


Figure 8. The energy distribution of the transferred electron for the ion speed of $1.5 \times 10^5 \text{ m s}^{-1}$ in figure 7(a) and $2.5 \times 10^5 \text{ m s}^{-1}$ in figure 7(b); these speeds correspond to scaled speeds of 0.82 and 1.37 of figure 6. Within each graph, each energy distribution has been scaled by the same factor. The line types are the same as in figure 6.

between the potentials were at small r which is not accessed when the electron has larger L .

6. Conclusions

We have performed classical calculations of an electron in non-Coulombic potential plus a static electric field to show that the classical behaviour mimics that in the fully quantum system. We found that the sign of the dipole resulting from a slowly increasing electric field depended on whether the potential was more or was less attractive than pure Coulomb if the system started in a low angular momentum state. We developed a simple map that reproduced this effect. This classical property is the result of the direction of precession of the Runge–Lenz vector due to the non-Coulombic potential. Classical calculations of charge transfer from highly excited states showed that this effect could lead to substantial changes in the charge transfer cross section; there were also substantial changes to the energy and angular momentum distributions of the transferred electron.

Acknowledgments

This work was supported by the Chemical Sciences, Geosciences, and Biosciences Division of the Office of Basic Energy Sciences, US Department of Energy.

References

- [1] Hezel T P, Burkhardt C E, Ciocca M, He L and Leventhal J J 1992 *Am. J. Phys.* **60** 329
- [2] Murray-Krezan J 2008 *Am. J. Phys.* **76** 1007
- [3] Freeman R R, Economu N P, Bjorkland G C and Lu K T 1978 *Phys. Rev. Lett.* **41** 1463
- [4] Harmin D 1982 *Phys. Rev. A* **26** 2656
- [5] Gao J, Delos J B and Baruch M 1992 *Phys. Rev. A* **46** 1449
- [6] Courtney M, Spellmeyer N, Jiao H and Kleppner D 1995 *Phys. Rev. A* **51** 3604
- [7] Dando P A, Monteiro T S, Delande D and Taylor K T 1996 *Phys. Rev. A* **54** 127
- [8] Keeler M L 2007 *Phys. Rev. A* **76** 052510
- Keeler M L 2008 *Phys. Rev. A* **77** 034503
- [9] Shan-Hong D, Song G, Yong-Ping L, Xue-You X and Sheng-Lu L 2010 *Chin. Phys. B* **19** 040511
- [10] Lankhuijzen G M and Noordam L D 1996 *Phys. Rev. Lett.* **76** 1784
- [11] Robicheaux F and Shaw J 1996 *Phys. Rev. Lett.* **77** 4154
- [12] Naudeau M L, Sukenik C I and Bucksbaum P H 1997 *Phys. Rev. A* **56** 636
- [13] Campbell M B, Bensity T J and Jones R R 1999 *Phys. Rev. A* **59** R4117
- [14] Texier F 2005 *Phys. Rev. A* **71** 013403
- [15] de Kertanguy A, Percival I C and Richards D 1981 *J. Phys. B: At. Mol. Opt. Phys.* **14** 641
- [16] Perotti L 2006 *Phys. Rev. A* **73** 053405
- [17] Hooker A, Greene C H and Clark W 1997 *Phys. Rev. A* **55** 4609
- [18] Gallagher T F 1994 *Rydberg Atoms* (Cambridge: Cambridge University Press)
- [19] Robicheaux F, Wesdorp C and Noordam L D 2000 *Phys. Rev. A* **62** 043404
- [20] Dando P A, Monteiro T S, Jans W and Schweizer W 1994 *Prog. Theor. Phys. Suppl.* **116** 403
- [21] Hupper B, Main J and Wunner G 1996 *Phys. Rev. A* **53** 744
- [22] MacAdam K B, Rolfes R and Crosby D A 1981 *Phys. Rev. A* **24** 1286
- [23] Rolfes R G, Smith D B and MacAdam K B 1988 *Phys. Rev. A* **37** 2378
- [24] MacAdam K B, Gray L G and Rolfes R G 1990 *Phys. Rev. A* **42** 5269
- [25] Percival I C and Richards D 1977 *J. Phys. B: At. Mol. Phys.* **10** 1497
- [26] Ehrenreich T, Day J C, Hansen S B, Horsdal-Pedersen E, MacAdam K B and Mogensen K S 1994 *J. Phys. B: At. Mol. Opt. Phys.* **27** L383
- [27] Wang J and Olson R E 1994 *Phys. Rev. Lett.* **72** 332
- [28] Cavagnero M J 1995 *Phys. Rev. A* **52** 2865
- [29] Vrinceanu D and Flannery M R 2000 *Phys. Rev. Lett.* **85** 4880
- [30] Press W H, Teukolsky S A, Vetterling W T and Flannery B P 1992 *Numerical Recipes* 2nd edn (Cambridge, MA: Cambridge University Press)
- [31] Donnan P H, Niffenegger K, Topcu T and Robicheaux F 2011 *J. Phys. B: At. Mol. Opt. Phys.* **44** 184003